Single-Walled Black Phosphorus Nanotube as a NO$_2$ Gas Sensor

Pengfei Ou [a,b,*], Xiao Zhou [c], Xiao-Yan Li [b], Yiqing Chen [a], Cheng Chen [d], Fanchao Meng [e], Jun Song [a,**]

[a] *Department of Mining and Materials Engineering, McGill University, Montreal H3A0C5, Quebec, Canada*
[b] *Department of Electrical and Computer Engineering, University of Toronto, Toronto M5S1A4, Ontario, Canada*
[c] *Institute of Mechanical Engineering, École Polytechnique Fédérale de Lausanne, Vaud, Lausanne CH-1015, Switzerland*
[d] *School of Aeronautics, Northwestern Polytechnical University, Xi'an 710072, Shaanxi, People's Republic of China*
[e] *Institute for Advanced Studies in Precision Materials, Yantai University, Yantai 264005, Shandong, People's Republic of China*

ARTICLE INFO

ABSTRACT

An *ab initio* density functional theory study on the candidacy of single-walled black phosphorus nanotubes (BPNTs) towards sensing several common toxic gas molecules (NH$_3$, CO, NO, NO$_2$, and SO$_2$) was conducted. Various adsorption characteristics, including the geometry, adsorption energy, charge transfer, band structure, and curvature effect were examined. Compared with MLBP, BPNTs are found to generally exhibit similar adsorption energy towards these molecules, whereas show selectively much stronger interaction with NO$_2$. Analysis of charge density difference and band structure also indicates the electronic properties of BPNTs are significantly altered after the adsorption of NO$_2$: transferring an indirect band gap of ~0.3 eV for pristine (0, 9) BPNT to a metallic system. These facts collectively indicate the higher capability, sensitivity, and selectivity of BPNTs in the detection of NO$_2$ compared to its planar counterpart. Moreover, the NO$_2$ adsorption is found to be influenced by the curvature of BPNTs. Overall, findings from the present study indicate that BPNTs may serve as potential building blocks for high-performance gas sensors towards NO$_2$ sensing.

1. Introduction

Two-dimensional (2D) black phosphorus (BP) is the most thermodynamic stable one in 2D phosphorus allotropes with an orthorhombic puckered structure. Few-layer BP exhibits many unique electronic/optical properties, including thickness-dependent direct band gap varying from 0.91 eV for monolayer to 0.28 eV for five layers [1], a high hole mobility of up to 1 000 cm^2 V^{-1} s^{-1} that exceeds the graphene or transition metal dichalcogenides [2], thickness-dependent on/off ratio over 10^4 [3–5], and strong in-plane anisotropy^5 resulted from its orthorhombic puckered structure. Additionally, these attractive characteristics could be further modulated by strain engineering [6–9], nanostructuring [10–13], chemical modification [14–16], and electric gating [4,17–20]. As a narrow band gap semiconductor with high carrier mobility and photoelectric conversion characteristics [21], BP has been applied in a variety of biosensors, such as fluorescence, electrochemical, field-effect transistor, chemiluminescence, and electrogenerated chemiluminescence biosensors [22–24]. In actuality, BP not only exhibits

photothermal response characteristics [25,26] but also has photoluminescence characteristics which realizes the application of fluorescent probes in biomedical imaging [27]. In addition to its sensitive photonic response characteristics, another major feature of two-dimensional BP is its enormous loading capacity of chemotherapy drugs and gene fragments due to its large specific surface area, to realize antitumor therapy and gene therapy [28].

The afore-mentioned properties of BP promise great opportunities in a wide range of applications [29,30], among which one application receiving particular attention is chemical sensing. It has been demonstrated by several density functional theory (DFT) studies, that monolayer BP (MLBP) would offer superior chemical sensing performance towards various chemicals, e.g., NO and NO$_2$ [14,31], with comparable or even higher molecular adsorption energy than other high-profile 2D materials such as graphene or MoS$_2$. Meanwhile, benefiting from its orthorhombic puckered structure, MLBP exhibits a larger surface-to-volume ratio than other planar 2D materials, which contributes to maximizing the adsorption effect and subsequently enhancing

---

the sensitivity of the channel material [32]. In addition, BP exhibits a much reduced out-of-plane electrical conductance, which may render an enhanced response signal to the target analytes when adsorbed on the surface [33]. Furthermore, MLBP also features direction-selective current-voltage characteristics[14] which is beneficial for chemical sensing.

On the other front, 2D materials are also prominent for their structural tunability by easily converting the planar structure into 1D nanotubes or nanoribbons. Some possible disadvantages of BPNTs are expected to be, being harmful to the environment and toxic to animals and humans; the synthesis of BPNTs suffers from the high cost of production since it requires novel synthetic methods and delicate experimental conditions. Despite their disadvantages, compared with the planar counterparts, the surface structure of nanotubes renders uniquely higher sensitivity which originates from their reduced dimensionality and unparalleled surface-to-volume ratio [34]. In addition, the tunable electronic/optical properties and structural stability of nanotubes make them appealing candidates in various applications, and particularly trigger the exploration and development of chemical and biological sensors [35]. Single-walled BP nanotubes (BPNTs) have been predicted to be possible by theoretical calculations [36–38], and further initiated several studies on their unique and tunable properties. More recently, the MLBP was predicted to maintain its stability under a tensile strain of up to 30% by DFT calculations[7] due to its small Young's modulus [6], which renders BPNTs worth exploring. Besides, it was found that both zigzag and armchair BPNTs show indirect band gap, and zigzag BPNTs can achieve semiconducting to semi-metallic transitions, whereas armchair BPNTs always behave as semiconductors, exhibiting highly anisotropic electronic behaviors [12]. The electronic properties of BPNTs can also be tuned from semiconducting to metallic via applying strain and electric field [10]. Recently, based on the numerical simulations via molecular dynamics, Shi et al [39]. discovered that a wider BP nanoribbon can self-assemble into chiral nanotubes with different radii upon carbon nanotubes, which provides a possibility of potential fabrication for the BPNTs. Intrigued by all of these, it is necessary to take a step further to bridge the gap between 0D and 2D BP-based nanostructures, and further explore the potential of BPNTs as the channel material in a chemical sensor.

Herein, a comparative study of various adsorption characteristics when various toxic gas molecules adsorbed on the outer surface of MLBP and BPNTs was performed, including NH_3, CO, NO, NO_2, and SO_2. First, we determined the preferential binding positions and corresponding adsorption energies. It is demonstrated that the binding strength is highly correlated with the amount of transferred charge between the P surface (i.e., MLBP and BPNTs) and adsorbed gas molecules. The BPNTs are more selectively sensitive than MLBP regarding the gas sensing for NO_2. The adsorptions on MLBP or BPNTs are generally stronger than graphene and MoS_2, which inclines to generate an enhanced effect on the electronic properties of the host layer, rendering them a more sensitive gas sensor. Particularly, the curvature effect on detecting gas molecules was also examined comparatively, through modeling BPNTs with various diameters. To our knowledge, no previous studies have reported on these issues theoretically or experimentally.

2. Computational method

2.1. DFT calculations

DFT calculations were performed by Vienna *Ab initio* Simulation Package (VASP) [40,41] to study the mechanisms of the common toxic gas molecules (NH_3, CO, NO, NO_2, and SO_2) adsorbed on the BPNTs and MLBP. The spin-polarization effect was considered for the cases of paramagnetic gas molecules, i.e., NO and NO_2, whereas it has not been included in the calculations of other gas molecules. The generalized gradient approximation was adopted to treat the exchange-correlation functional as parametrized by Perdew-Burke-Ernzerhof (PBE) [42]. The plane-wave energy cut-off was chosen as 500 eV and the *k*-point

grids were set to $1 \times 1 \times 3$ and $4 \times 4 \times 1$ for BPNTs and MLBP, respectively. The adsorption geometries were optimized by using a conjugate gradient algorithm, and the structural relaxation was converged until the Hellmann-Feynman force on each of the ions fell under 0.01 eV Å^{-1}. The empirical correction of the DFT-D2 method of Grimme was included for a better description of the weak van der Waals force [43]. We first optimized the lattice constants of BPNTs and MLBP without the adsorbates, and then fixed the volume and shape of our slab models with only the positions of atoms to move when relaxing the geometries of BPNTs and MLBP with the adsorbates.

2.2. Modeling the BPNTs and MLBP

BPNTs can be constructed by rolling up a MLBP, with a pair of integer indexes (m, n) to describe, indicating their diameter and chirality. Indexes of $(m, 0)$ and $(0, n)$ represent zigzag and armchair nanotubes, respectively (see Fig. 1a). In the present study, we only considered the BPNTs along armchair direction due to the structural instability of BPNTs along the zigzag direction post adsorption (more details can be found in Supplementary Fig. 1). Particularly, the 1D (0, 9)BPNT was chosen as a representative example for most of the calculations on the BPNTs, meanwhile (0, 8), (0, 10), (0, 11), and (0, 12)BPNTs were also included to study the curvature effect in the last section. We also examined the results on MLBP to have a direct comparison with those on BPNTs, which is modeled as a $4 \times 3 \times 1$ monolayer sheet containing 48 P atoms. For calculations of BPNTs and MLBP, minimum separation distances of 20 Å between neighboring periodic images were used to ensure negligible interaction between periodic images across the periodic boundaries.

2.3. Adsorption geometry and energy

For simplicity, we only considered one gas molecule adsorbed onto the outer surface of the BPNTs or the basal plane of MLBP. The adsorption strength of a certain gas molecule is evaluated by examining the adsorption energy, defined as Eq. (1):

$$E_{ad} = E(\text{gas/substrate}) - E(\text{gas}) - E(\text{substrate}) \tag{1}$$

where $E(\text{gas/substrate})$, $E(\text{gas})$, and $E(\text{substrate})$ denote the energy of BPNT/MLBP with an adsorbed gas molecule, an isolated gas molecule, and BPNT/MLBP, respectively. A negative E_{ad} indicates an exothermic adsorption process that is energetically favored, whereas a positive value refers to the opposite scenario. We note that for the calculations of isolated gas molecules, one gas molecule was placed in a periodic cubic box with more than 20 Å in length for each dimension and gamma-only *k*-point of Brillouin zone was used to determine the energy.

We screened various orientations of a gas molecule at different adsorption locations on MLBP and BPNTs to determine the optimized adsorption sites and molecule orientations. Specifically, three different adsorption locations exhibiting high structural symmetry were considered, i.e., Hollow (H) site (a hexagon hollow), Top (T) site (top of a P atom), and Bridge (B) site (between a P−P bond that forms a certain angle) (as illustrated in Fig. 1c). A similar strategy was used in identifying potential adsorption sites for gas molecule adsorption on MLBP.

3. Results and discussion

3.1. Atomic structures of MLBP and BPNTs

We first examined the atomic structures of MLBP and BPNTs. Starting from the benchmarking MLBP system, we confirm it to exhibit a puckered honeycomb lattice structure of the space group of *Cmca* (no. 64) and Pearson symbol of *oC*8, as shown in Fig. 1a, in agreement with the previous studies[44]. In such puckered structure, P atoms are essentially located in two parallel sublayers, with the distance between the
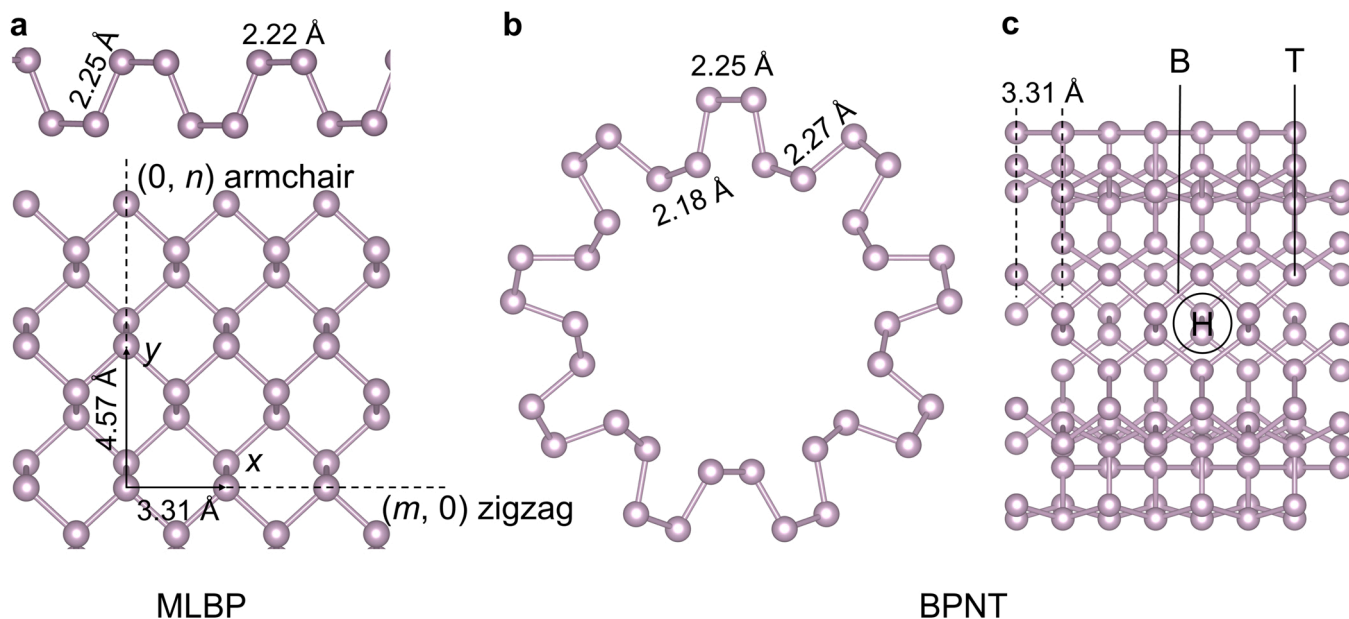
Fig. 1. (a) Side view (first row) and top view (second row) of a MLBP sheet with geometrical parameters indicated. BPNTs are then constructed via rolling up of the MLBP sheet with the roll-up vector of $\vec{R} = m\vec{x} + n\vec{y}$, where x and y denote the zigzag and armchair directions, respectively. (b) Top and (c) side views of the atomic structure of (0, 9)BPNT along the armchair direction. Three sites for gas molecule adsorption identified on the BPNT were denoted as H site (a hexagon hollow), T site (top of a P atom), and B site (between the P−P bond that forms a certain angle).

two sublayers denoted as the puckered height. Each P atom binds with three other P atoms, within which, three out of four are sitting in one plane while one is located at the adjacent parallel plane. The lattice constants of MLBP are optimized to be $a = 3.31$ Å and $b = 4.57$ Å respectively, and the puckered height is determined to be 2.11 Å. The optimized bond lengths of P−P bonds are 2.22 Å and 2.25 Å for the bonds in horizontal and vertical directions, respectively. The bond angles at each P atom in monolayer BP are added up to 303.78°, close to the idealized value of 328° for the sp^3 (tetrahedral) hybridization and much smaller than 360° for sp^2 (planar) hybridization. Constructed from the MLBP, models of BPNTs were developed. The case of the (0, 9)BPNT as a representative is illustrated in Fig. 1b,c with its side and top views along the armchair direction depicted. The puckered height in (0, 9) BPNT is slightly increased to 2.27 Å together with the optimized bond length of P−P in the inner sublayer remains intact, also it increases from 2.22 to 2.25 Å for the outer sublayer. The lattice constant along the tube axis is also 3.31 Å for (0, 9)BPNT which is equivalent to that of MLBP

along zigzag direction.

3.2. Adsorption geometry and energy

We also benchmarked the adopted computational method by comparing our results with the existing literature data of isolated gas molecules. After relaxations, the calculated bond lengths of NH$_3$, CO, NO, NO$_2$, and SO$_2$ are 1.02, 1.14, 1.17, 1.21, and 1.45 Å, respectively, while the bond angles for the non-linear molecules, i.e., NH$_3$, NO$_2$, and SO$_2$, are 106.62°, 133.90°, and 119.25°, respectively. These values are in good agreement with the reported experimental and theoretical values in the previous studies [45,46]. In addition to the structural parameters, the total magnetic moment when magnetic NO and NO$_2$ adsorbed on BPNTs and MLBP were calculated to be 1 μ_B, which is similar to the theoretical results that were reported on the adsorption of monolayer MoS$_2$ [47].

As illustrated in Fig. 2, for MLBP, NO has the largest adsorption
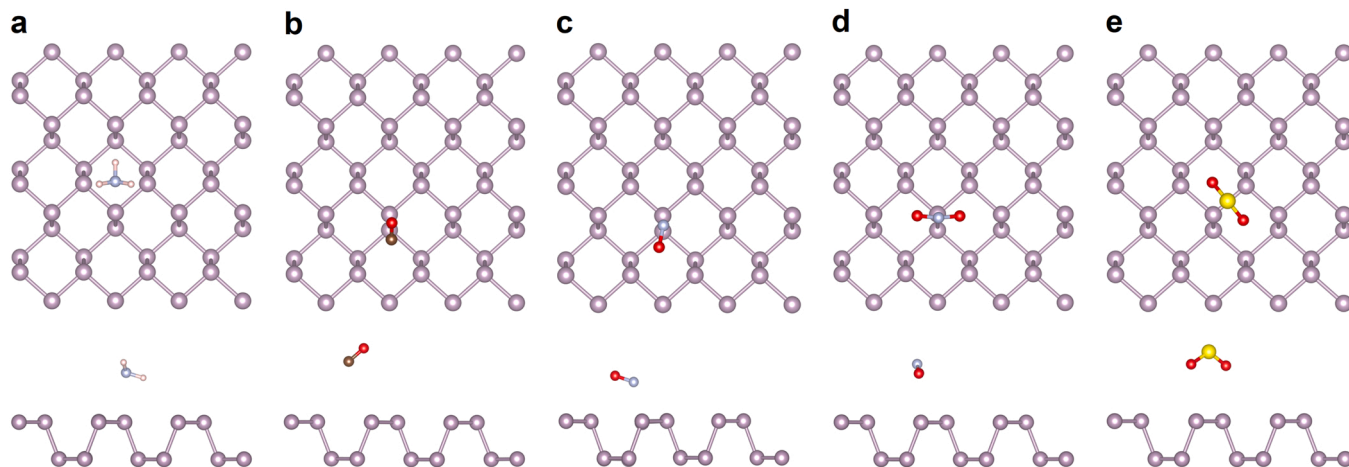
Fig. 2. Top and side view of the optimized geometries of (a) NH$_3$, (b) CO, (c) NO, (d) NO$_2$, and (e) SO$_2$ adsorbed on the basal plane of MLBP are provided in the first and second row, respectively. Purple, P; yellow, S; red, O; silver, N; brown, C; pink, H.

energy of −295.03 meV amongst various gas molecules, which agrees well with the recent theoretical results[14] and also confirmed the candidacy of MLBP being applied as the potential channel material in a NO gas sensor. The value of E_{ad} for NO$_2$ (−243.2 meV) adsorbed onto the MLBP agrees well with the previous theoretical result based on the GGA functional (−273 meV) [31]. Additionally, the E_{ad} values for NH$_3$, CO, and SO$_2$ are −203.4, −77.3, and −127.4 meV, respectively. The calculation results suggest that all gas molecules physically adsorb on MLBP since the E_{ad} is generally smaller than −500 meV. No notable variations of bond lengths (Δb) (less than 0.02 Å) in optimized geometries are observed for all gas molecules. For the non-linear gas molecules of NH$_3$ and SO$_2$, the bond angles remain unchanged before and after the adsorption, except for NO$_2$. CO, NO, and NO$_2$ preferentially adsorb at the T site, among others; however, the NH$_3$ is found to be most stable with its center of mass located at the H site. Meanwhile, SO$_2$ is almost parallel aligning with the P layer with the S atom sitting on top of the P−P bond.

We further examined the circumstances of these gas molecules absorbed on (0, 9)BPNT. As shown in Fig. 3, remarkable differences in the adsorption geometries were observed for different gas molecules. Specifically, (a) NH$_3$ and CO molecules favor the adsorption at the B site, with N−H and C−O bond length of 1.02 Å and 1.14 Å, respectively; (b) the N atom in NO and O atom in NO$_2$ adsorb close to the (0, 9)BPNT, and T site is the most energetically favored adsorption site with an adsorption energy of −240.71 and −537.20 meV, respectively. The bond angle of NO$_2$ after adsorption is 118.67°, a large distortion compared to that of 133.90° in its isolate gas state, indicating a relatively strong interaction between NO$_2$ and (0, 9)BPNT. The adsorption energies decrease from NO$_2$ to CO and follow the sequence of NO$_2$ > NO > SO$_2$ > NH$_3$ > CO. Obviously, the E_{ad} values for NO and NO$_2$ on (0, 9)BPNT are different from those on MoS$_2$ nanotubes. For NO and NO$_2$, the E_{ad} values on (0, 9) BPNT are predicted to be −240.71 and −537.20 meV, which are much larger than that on MoS$_2$ nanotubes with −129.3 and −35.6 meV, respectively. Since higher adsorption energy results in a strong binding between the adsorbates and substrate, we expect that the interaction between NO or NO$_2$ and BPNTs are much stronger than that of MoS$_2$ nanotubes.

Next, it is significant to make a comparison between the key characteristics of CO, NH$_3$, NO, NO$_2$, and SO$_2$ adsorbed onto the MLBP and (0, 9)BPNT. For both systems, the adsorption energies are smaller than 1 eV, indicating the adsorption strength is between the strong physisorption and weak chemisorption. The E_{ad} value of NO$_2$ adsorption on (0, 9)BPNT (−537.20 meV) is more than two times higher than that of MLBP (−243.2 meV), which reflects a much stronger interaction between the NO$_2$ and (0, 9)BPNT. In previous studies, MLBP has been developed to achieve a highly selective response to paramagnetic NO$_2$ when operating under room temperature [31,48,49], along with an ultrafast response time and a high sensitivity that detects the analytes at ppb levels [31]. Previous theoretical calculations also suggest that the selective response of BP can also be realized owing to its larger molecular adsorption energy compared to other 2D nanomaterials, such as MoS$_2$ and graphene [31]. Therefore, it is predicted that the BPNTs could enhance the adsorption capability, sensitivity, and selectivity of FET gas sensors in detecting NO$_2$ gas.

We employed the Bader charge analysis [50–53] to analyze the charge distribution and elucidate the nature of interactions between BPNT/MLBP and adsorbed gas molecules; thus, to explore the charge transfers induced by the adsorption. The charge density differences were determined by the following Eq. (2).

$$\Delta\rho(z) = \rho(\text{gas/substrate}) - \rho(\text{gas}) - \rho(\text{substrate}) \tag{2}$$

where substate denotes the (0, 9)BPNT or MLBP, and gas represents the gas molecules of NH$_3$, CO, NO, NO$_2$, and SO$_2$. The iso-surface images of charge density differences are depicted in Fig. 4 for NH$_3$, CO, NO, NO$_2$, and SO$_2$ molecules adsorbed on (0, 9)BPNT with the light yellow and blue regions denote the charge accumulation and depletion, respectively. As shown in Table 1, a positive ΔQ means the charge is transferred from the adsorbed gas molecules to BPNT/MLBP; and vice versa. The trend of gaining or losing electrons for NH$_3$, CO, NO, NO$_2$, and SO$_2$ is similar on both BPNT and MLBP, that is, a noticeable charge depletion is observed when CO, NO, NO$_2$, CO, and SO$_2$ are adsorbed on the outer surface of (0, 9)BPNT revealing that they are acting as charge acceptors and withdrawing the electrons from (0, 9)BPNT, except for NH$_3$ behaves oppositely by donating electrons to (0, 9)BPNT. This agrees well with the theoretical findings in the previous studies that, NO and NO$_2$ are withdrawing electrons, and NH$_3$ is donating electrons to either
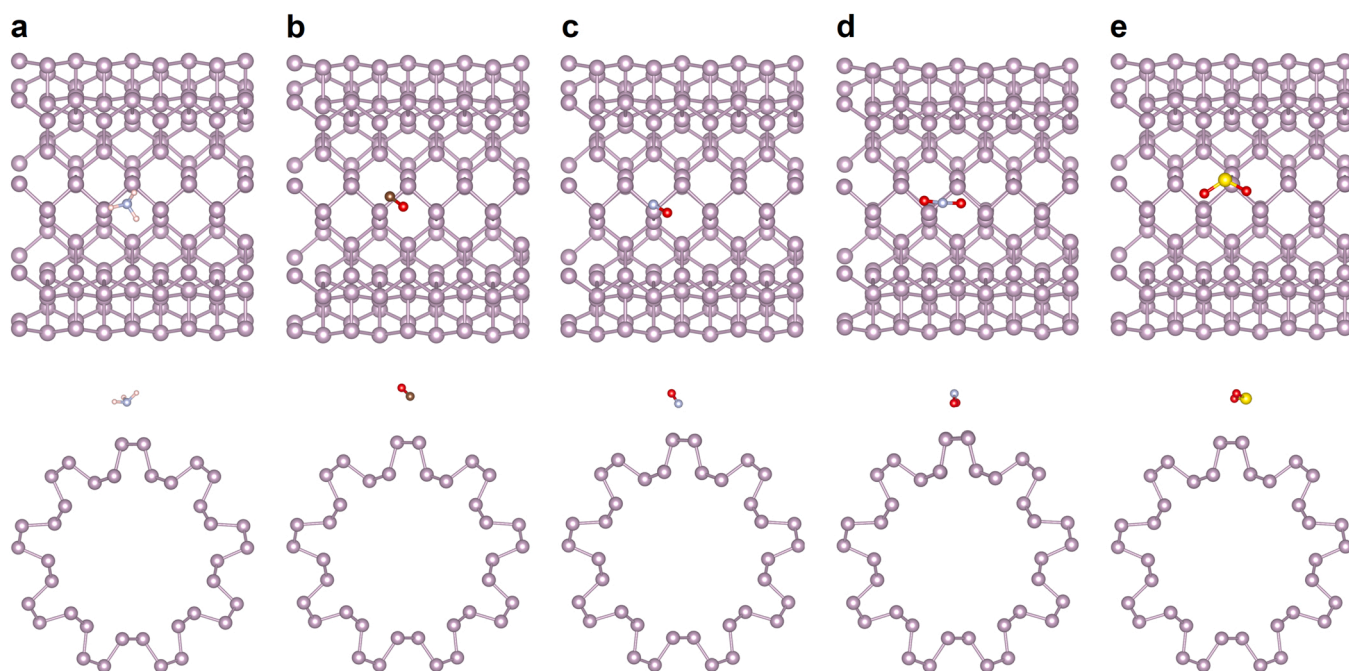
Fig. 3. Top and side view of the optimized geometries of (a) NH$_3$, (b) CO, (c) NO, (d) NO$_2$, and (e) SO$_2$ adsorbed on the outer surface of (0, 9)BPNT are provided in the first and second row, respectively. Purple, P; yellow, S; red, O; silver, N; brown, C; pink, H.
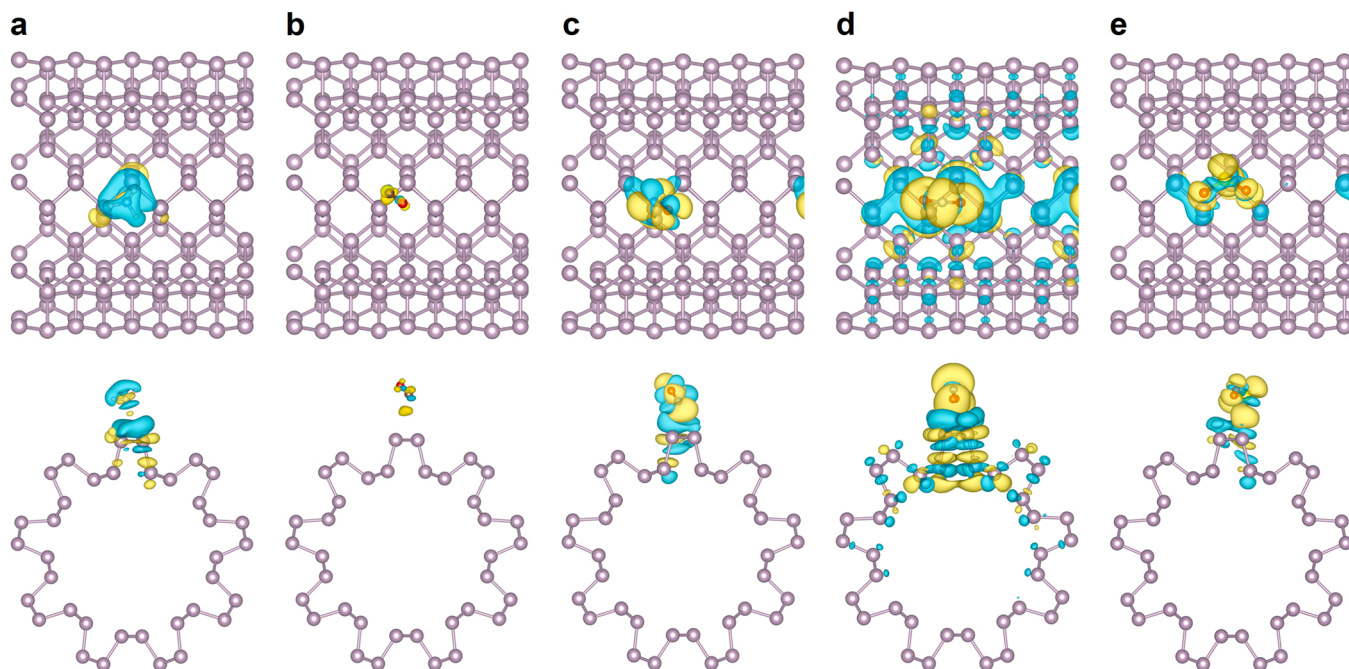
Fig. 4. Top and side view of the iso-surface plots of charge density difference for (a) NH_3, (b) CO, (c) NO, (d) NO_2, and (e) SO_2 adsorbed on the outer surface of (0, 9) BPNT are provided in the first and second row, respectively. Purple, P; yellow, S; red, O; silver, N; brown, C; pink, H. The light yellow and blue shaded regions respectively correspond to the charge accumulation and depletion with the iso-surface level is set to 0.0005 e/Bohr^3.

Table 1

Various adsorption characteristics of different gas molecules before and after the adsorption onto (0, 9)BPNT and MLBP. The bond length of the free molecule (b, in Å), the change of bond length (Δb, in Å) and bond angle ($\Delta\theta$), the adsorption energy (E_{ad}, in meV), and the charge transfer from (0, 9)BPNT/MLBP to the gas molecule (ΔQ, in e). Negative ΔQ means the gas molecule acts as an electron donor and gives electrons away to the (0, 9)BPNT/MLBP.

|	Isolated gas		(0, 9)BPNT				MLBP			
	b	θ	Δb	$\Delta\theta$	ΔQ	E_{ad}	Δb	$\Delta\theta$	ΔQ	E_{ad}
NH_3	1.02	106.62	−0.001	1.00	−0.04	−189.30	−0.001	0.98	−0.017	−203.40
CO	1.14	/	0.001	/	0.02	−85.45	0.001	/	0.020	−77.28
NO	1.17	/	0.01	/	0.15	−240.71	0.02	/	0.221	−295.03
NO_2	1.21	133.90	0.05	−15.23	0.55	−537.20	0.01	−5.77	0.214	−243.18
SO_2	1.45	119.25	0.01	−1.37	0.16	−221.92	0.001	−0.30	0.031	−127.40

monolayer MLBP [14,49] or monolayer MoS_2 [45–47].

The value of transferred charge between BPNT/MLBP and gas molecules is an essentially important factor determining the sensitivity of a FET sensor [49]. The higher value of transferred charge would result in greater variation in the conductivity of the channel material, and thus more sensitive the sensor. Specifically, NO_2 acts as charge-acceptor and accepts 0.55 e from the (0, 9)BPNT, which is significantly larger than that on MLBP with a value of 0.21 e. This agrees well with the fact that the adsorption energy of NO_2 on (0, 9)BPNT (−537.20 meV) is remarkably higher than that of on MLBP (−243.18 meV). We also calculated the band structures of (0, 9)BNPTs with the adsorption of these gas molecules and compared them to that of pristine (0, 9)BNPT. It also confirms the tendency observed from Bader charge analysis, that is, the electronic properties are significantly altered after the adsorption of NO_2, transferring an indirect band gap of 0.32 eV for pristine (0, 9)BPNT to a metallic system, as profiled in Fig. 5. A great amount of charge transfer and significant band alteration in the NO_2 adsorption on (0, 9) BPNT compared to that of MLBP, which indicates that the BPNT shows greater sensitivity than MLBP when assembled into a NO_2 gas sensor. Charge transfer between analytes and 2D nanomaterials can thus induce the variation in the conductance of BP FETs with varying concentrations. Given that the analytes trap electrons from BP in a gas sensor, it would reduce the concentration of electrons in the conduction band, and result in an increased resistivity of BP. On the contrary, the resistance of

BP would increase if the analytes contribute electrons to BP in a gas sensor. On the basis of theoretical results obtained in the present study, we conclude that different operations should be applied to detect various gas molecules which originated from different charge transfer behavior. A more positive gate voltage is thus needed to operate the BPNT gas sensors by using FET in the detection of gas molecules of NO_2, and SO_2. In contrast, a low gate voltage is required when detecting the NH_3.

3.3. Curvature and strain engineering

The different behaviors and energies observed for gas molecules adsorbed on MLBP and BPNTs might be attributed to the curved surfaces in BPNTs, and the straining endured by the BP sublayers in the curved state. To elucidate the curvature effect on the adsorption capability of BPNTs towards adsorbates, we further examined the characteristics of gas molecule adsorption on the BPNTs with different curvatures. Specifically, we further selected multiple BPNTs with diameters ranging from (0, 8), (0, 10), (0, 11), to (0, 12), and performed similar calculations by placing the studied gas molecules on the outer surface of these BPNTs in the similar geometries as on (0, 9)BPNT. By comparing the results obtained for various BPNTs and MLBP (regarded as BPNT with infinite diameter), for NO_2, the adsorption energies are sensitive to the curvature of BPNTs due to strong adsorption between NO_2 and BPNTs;
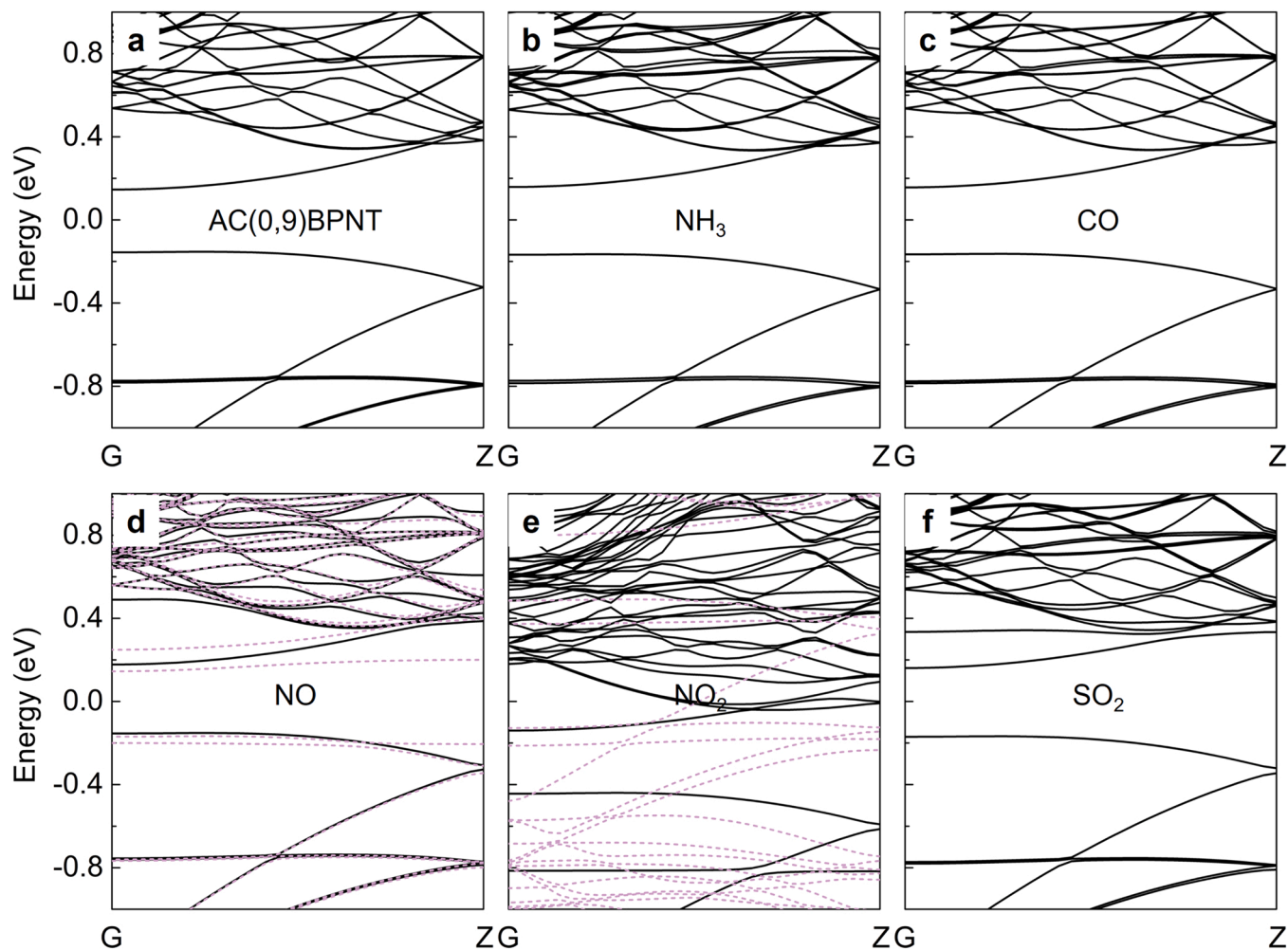
**Fig. 5.** Band structures of (a) pristine (0, 9)BPNT and (0, 9)BPNT after the adsorption of (b) NH$_3$, (c) CO, (d) NO, (e) NO$_2$, and (f) SO$_2$. High symmetry points of G and Z in the band structures correspond to the (0, 0, 0) and (0, 0, 0.5) in the Brillouin zone, respectively. The spin-up and spin-down component of band structure when NO and NO$_2$ adsorbed on (0, 9)BPNT are represented by black solid line and purple dashed line, respectively.

however, the adsorption of other gas molecules is insensitive to the curvature effect, as shown in Fig. 6a.

Since BPNTs are constructed by rolling up a MLBP, the intrinsic strain in BPNT usually renders larger bond lengths of P−P bonds compared to its monolayer. To provide an intuitive understanding of the strain effect on the adsorption energy, the adsorption of NO$_2$ on a corrugated MLBP, which is equal to having an anisotropic compressive strain artificially applied, was also studied. As shown in Fig. 6b, the NO$_2$

adsorption energy is significantly enhanced on the corrugated MLBP compared to that of the pristine one (−604.4 meV vs. −243.2 meV), which is comparable to the values obtained on (0, 9)BPNTs. We also notice that the recent study by Jeong et al [54]. reported that the response and sensitivity of a graphene sensor would be much enhanced by using the self-corrugated graphene, where the wrinkled surfaces of graphene are stemmed from the strain-induced structure modifications. We conclude that the compressive or tensile strain has an obvious effect
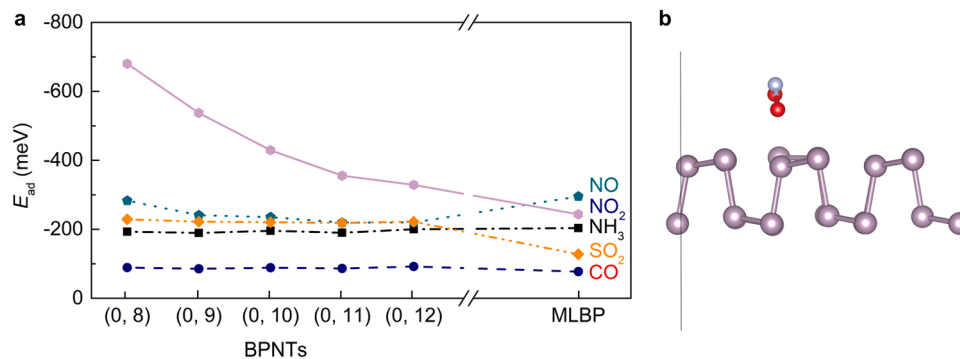
Fig. 6. (a) The adsorption energy (E_{ad} in meV) when NH$_3$, CO, NO, NO$_2$, and SO$_2$ adsorbed on various diameters of (0, 8), (0, 9), (0, 10), (0, 11), and (0, 12)BPNTs (solid geometric symbols), compared with MLBP (nanotube with an infinite diameter). (b) Optimized geometry of NO$_2$ adsorption on the corrugated MLBP. Purple, P; red, O; silver, N.

on the NO$_2$ sensing capability of a BP gas sensor. Further efforts should be devoted to the studies regarding strain engineering on the adsorption behavior.

4. Discussion

In the present study, we only considered single adsorbates in determining the adsorption strength, charge transfer, and electronic band structure when NH$_3$, CO, NO, NO$_2$, and SO$_2$ adsorbed on BPNTs. Yet we expect the co-existence between multiple analytes for a real-life sensing application, and the competitive adsorption and mutual interaction will effectively affect the performance of a FET-based gas sensor if we need to obtain a more accurate assessment of capability, sensitivity, and selectivity. We further note that studies on the transport properties, including the device simulations to calculate the *I-V* characteristics, transport spectrum, vertical Schottky-barrier height, etc., would be significant aspects of our future studies down the road. Moreover, heterostructure engineering [23,55,56], defect engineering [57,58], and surface functionalization [59–61] may hold the possibility of modifying the properties of BPNTs and affecting their interaction with analytes. All these challenges, require additional research efforts and further development of new computational frameworks and experimental verifications.

5. Conclusions

In summary, this study estimates the candidacy of BPNTs on chemical sensing the toxic gas molecules (i.e., NH$_3$, CO, NO, NO$_2$, and SO$_2$) by *ab initio* DFT calculations. Various adsorption sites and orientations were systematically investigated to determine the most favorable geometry. Our results demonstrate that most gas molecules (except NO$_2$) are physiosorbed on the outer surface of BPNTs and behave as either charge donors or acceptors with a small amount of charge transfer. Further, compared to MLBP, the adsorption energy of NO$_2$ is selectively enhanced when interacting with BPNTs. From Bader charge analysis, the calculated charge transfer values between NO$_2$ and (0, 9)BPNT is multiple or dozen of times higher than others. The band structure is also significantly altered after the adsorption of NO$_2$, transferring an indirect band gap of ~0.3 eV for pristine (0, 9)BPNT to a metallic system. We note that the BPNTs would have higher capability, sensitivity, and selectivity than its monolayer in the detection of NO$_2$. The curvature effect on the adsorption characteristics of BPNT also has been explored. We found that, for NO$_2$, the adsorption energy can be enhanced by either choosing a BPNT with a smaller diameter or applying compressive strain, whereas the adsorption of other gas molecules is insensitive to these effects. Overall, our results suggest the promise of BPNTs as a channel material in FETs in future NO$_2$ sensing applications.

CRediT authorship contribution statement

Pengfei Ou: Conceptualization, Methodology, Software, Formal analysis, Writing – original draft. **Xiao Zhou:** Software, Writing – review & editing. **Xiao-Yan Li:** Software, Writing – review & editing. **Yiqing Chen:** Software, Validation. **Cheng Chen:** Software, Validation. **Fanchao Meng:** Software, Validation. **Jun Song:** Conceptualization, Writing – review & editing, Supervision.

Declaration of Competing Interest

The authors declare that they have no known competing financial interests or personal relationships that could have appeared to influence the work reported in this paper.

Acknowledgements

Appendix A. Supporting information

Supplementary data associated with this article can be found in the online version at doi:10.1016/j.mtcomm.2022.103434.

References

[1] J. Qiao, X. Kong, Z.-X. Hu, F. Yang, W. Ji, High-mobility transport anisotropy and linear dichroism in few-layer black phosphorus, Nat. Commun. 5 (2014) 1–7.

[2] L. Li, Y. Yu, G.J. Ye, Q. Ge, X. Ou, H. Wu, D. Feng, X.H. Chen, Y. Zhang, Black phosphorus field-effect transistors, Nat. Nanotechnol. 9 (2014) 372–377.

[3] H. Liu, A.T. Neal, Z. Zhu, Z. Luo, X. Xu, D. Tománek, P.D. Ye, Phosphorene: an unexplored 2D semiconductor with a high hole mobility, ACS Nano 8 (2014) 4033–4041.

[4] S.P. Koenig, R.A. Doganov, H. Schmidt, A.H. Castro Neto, B. Özyilmaz, Electric field effect in ultrathin black phosphorus, Appl. Phys. Lett. 104 (2014), 103106.

[5] F. Xia, H. Wang, Y. Jia, Rediscovering black phosphorus as an anisotropic layered material for optoelectronics and electronics, Nat. Commun. 5 (2014) 1–6.

[6] Q. Wei, X. Peng, Superior mechanical flexibility of phosphorene and few-layer black phosphorus, Appl. Phys. Lett. 104 (2014), 251915.

[7] X. Peng, Q. Wei, A. Copple, Strain-engineered direct-indirect band gap transition and its mechanism in two-dimensional phosphorene, Phys. Rev. B 90 (2014), 085402.

[8] Z.-Y. Ong, Y. Cai, G. Zhang, Y.-W. Zhang, Strong thermal transport anisotropy and strain modulation in single-layer phosphorene, J. Phys. Chem. C. 118 (2014) 25272–25277.

[9] R. Fei, L. Yang, Lattice vibrational modes and raman scattering spectra of strained phosphorene, Appl. Phys. Lett. 105 (2014), 083120.

[10] H. Guo, N. Lu, J. Dai, X. Wu, X.C. Zeng, Phosphorene nanoribbons, phosphorus nanotubes, and van der waals multilayers, J. Phys. Chem. C. 118 (2014) 14051–14059.

[11] Q. Wu, L. Shen, M. Yang, Y. Cai, Z. Huang, Y.P. Feng, Electronic and Transport Properties of Phosphorene Nanoribbons, Phys. Rev. B 92 (2015), 035436.

[12] L. Guan, G. Chen, J. Tao, Prediction of the electronic structure of single-walled black phosphorus nanotubes, Phys. Chem. Chem. Phys. 18 (2016) 15177–15181.

[13] V. Tran, L. Yang, Scaling laws for the band gap and optical response of phosphorene nanoribbons, Phys. Rev. B 89 (2014), 245401.

[14] L. Kou, T. Frauenheim, C. Chen, Phosphorene as a superior gas sensor: selective adsorption and distinct *I–V* response, J. Phys. Chem. Lett. 5 (2014) 2675–2681.

[15] A. Ziletti, A. Carvalho, D.K. Campbell, D.F. Coker, Castro Neto, A. H., Oxygen Defects in Phosphorene, Phys. Rev. Lett. 114 (2015), 046801.

[16] V.V. Kulish, O.I. Malyi, C. Persson, P. Wu, Adsorption of metal adatoms on single-layer phosphorene, Phys. Chem. Chem. Phys. 17 (2015) 992–1000.

[17] J. Dai, X.C. Zeng, Bilayer phosphorene: effect of stacking order on bandgap and its potential applications in thin-film solar cells, J. Phys. Chem. Lett. 5 (2014) 1289–1293.

[18] J.E. Padilha, A. Fazzio, A.J.R. da Silva, Van Der Waals heterostructure of phosphorene and graphene: tuning the schottky barrier and doping by electrostatic gating, Phys. Rev. Lett. 114 (2015), 066803.

[19] Q. Liu, X. Zhang, L.B. Abdalla, A. Fazzio, A. Zunger, Switching a normal insulator into a topological insulator via electric field with application to phosphorene, Nano Lett. 15 (2015) 1222–1228.

[20] S. Das, M. Demarteau, A. Roelofs, Ambipolar phosphorene field effect transistor, ACS Nano 8 (2014) 11730–11738.

[21] F. Xia, H. Wang, D. Xiao, M. Dubey, A. Ramasubramaniam, Two-dimensional material nanophotonics, Nat. Photonics 8 (2014) 899–907.

[22] X. Ge, Z. Xia, S. Guo, Recent advances on black phosphorus for biomedicine and biosensing, Adv. Funct. Mater. 29 (2019), 1900318.

[23] R. Kumar, S. Pal, N. Pal, V. Mishra, Y.K. Prajapati, High-performance bimetallic surface plasmon resonance biochemical sensor using a black phosphorus–MXene hybrid structure, Appl. Phys. A 127 (2021) 259.

[24] M. Qiu, A. Singh, D. Wang, J. Qu, M. Swihart, H. Zhang, P.N. Prasad, Biocompatible and biodegradable inorganic nanostructures for nanomedicine: silicon and black phosphorus, Nano Today 25 (2019) 135–155.

[25] S. Chen, C. Xing, D. Huang, C. Zhou, B. Ding, Z. Guo, Z. Peng, D. Wang, X. Zhu, S. Liu, Eradication of tumor growth by delivering novel photothermal selenium-coated tellurium nanoheterojunctions, Sci. Adv. 6 (2020) eaay6825.

[26] Z. Xie, M. Peng, R. Lu, X. Meng, W. Liang, Z. Li, M. Qiu, B. Zhang, G. Nie, N. Xie, Black phosphorus-based photothermal therapy with aCD47-mediated immune checkpoint blockade for enhanced cancer immunotherapy, Light.: Sci. Appl. 9 (2020) 1–15.

[27] A. Castellanos-Gomez, L. Vicarelli, E. Prada, J.O. Island, K. Narasimha-Acharya, S.I. Blanter, D.J. Groenendijk, M. Buscema, G.A. Steele, J. Alvarez, Isolation and characterization of few-layer black phosphorus, 2D Mater. 1 (2014), 025001.

[28] F. Yin, K. Hu, S. Chen, D. Wang, J. Zhang, M. Xie, D. Yang, M. Qiu, H. Zhang, Z. Li, Black phosphorus quantum dot based novel siRNA delivery systems in human pluripotent teratoma PA-1 cells, J. Mater. Chem. B 5 (2017) 5433–5440.

[29] R. Gusmao, Z. Sofer, M. Pumera, Black phosphorus rediscovered: from bulk material to monolayers, Angew. Chem. Int. Ed. 56 (2017) 8052–8072.

[30] Y. Zhou, M. Zhang, Z. Guo, L. Miao, S.-T. Han, Z. Wang, X. Zhang, H. Zhang, Z. Peng, Recent advances in black phosphorus-based photonics, electronics, sensors and energy devices, Mater. Horiz. 4 (2017) 997–1019.

[31] S.-Y. Cho, Y. Lee, H.-J. Koh, H. Jung, J.-S. Kim, H.-W. Yoo, J. Kim, H.-T. Jung, Superior chemical sensing performance of black phosphorus: comparison with MoS$_2$ and graphene, Adv. Mater. 28 (2016) 7020–7028.

[32] S.J. Ray, M.V. Kamalakar, R. Chowdhury, *Ab initio* studies of phosphorene island single electron transistor, J. Phys.: Condens. Matter 28 (2016), 195302.

[33] A.N. Abbas, B. Liu, L. Chen, Y. Ma, S. Cong, N. Aroonyadet, M. Köpf, T. Nilges, C. Zhou, Black phosphorus gas sensors, ACS Nano 9 (2015) 5618–5624.

[34] H.-S.P. Wong, D. Akinwande, Carbon nanotube and graphene device physics, Cambridge University Press, 2011.

[35] I.V. Zaporotskova, N.P. Boroznina, Y.N. Parkhomenko, L.V. Kozhitov, Carbon nanotubes: sensor properties. a review, Mod. Electron. Mater. 2 (2016) 95–105.

[36] G. Seifert, E. Hernández, Theoretical prediction of phosphorus nanotubes, Chem. Phys. Lett. 318 (2000) 355–360.

[37] I. Cabria, J.W. Mintmire, Stability and electronic structure of phosphorus nanotubes, Europhys. Lett. 65 (2004) 82.

[38] T. Hu, A. Hashmi, J. Hong, Geometry, electronic structures and optical properties of phosphorus nanotubes, Nanotechnology 26 (2015), 415702.

[39] J. Shi, K. Cai, L.-N. Liu, Q.-H. Qin, Self-assembly of a parallelogram black phosphorus ribbon into a nanotube, Sci. Rep. 7 (2017) 12951.

[40] G. Kresse, J. Furthmüller, Efficiency of *Ab-Initio* total energy calculations for metals and semiconductors using a plane-wave basis set, Comput. Mater. Sci. 6 (1996) 15–50.

[41] G. Kresse, J. Furthmüller, Efficient iterative schemes for *Ab Initio* total-energy calculations using a plane-wave basis set, Phys. Rev. B 54 (1996) 11169–11186.

[42] J.P. Perdew, K. Burke, M. Ernzerhof, Generalized gradient approximation made simple, Phys. Rev. Lett. 77 (1996) 3865–3868.

[43] S. Grimme, Semiempirical GGA-type density functional constructed with a long-range dispersion correction, J. Comput. Chem. 27 (2006) 1787–1799.

[45] S. Zhao, J. Xue, W. Kang, Gas adsorption on MoS$_2$ monolayer from first-principles calculations, Chem. Phys. Lett. 595–596 (2014) 35–42.

[46] C. Rongfang, Z. Bo, J. Cuifang, Z. Xiaodong, J. Zhenyi, Theoretical study of the NO, NO$_2$, CO, SO$_2$, and NH$_3$ adsorptions on multi-diameter single-wall MoS$_2$ nanotube, J. Phys. D: Appl. Phys. 49 (2016), 045106.

[47] Q. Yue, Z. Shao, S. Chang, J. Li, Adsorption of gas molecules on monolayer MoS$_2$ and effect of applied electric field, Nanoscale Res. Lett. 8 (2013) 1–7.

[48] A.N. Abbas, B. Liu, L. Chen, Y. Ma, S. Cong, N. Aroonyadet, M. Köpf, T. Nilges, C. Zhou, Black phosphorus gas sensors, ACS Nano 9 (2015) 5618–5624.

[49] S. Cui, H. Pu, S.A. Wells, Z. Wen, S. Mao, J. Chang, M.C. Hersam, J. Chen, Ultrahigh sensitivity and layer-dependent sensing performance of phosphorene-based gas sensors, Nat. Commun. 6 (2015) 8632.

[50] G. Henkelman, A. Arnaldsson, H. Jónsson, A. Fast, Fast and robust algorithm for bader decomposition of charge density, Comput. Mater. Sci. 36 (2006) 354–360.

[51] E. Sanville, S.D. Kenny, R. Smith, G. Henkelman, Improved grid-based algorithm for Bader charge allocation, J. Comput. Chem. 28 (2007) 899–908.

[52] W. Tang, E. Sanville, G. Henkelman, A. Grid-Based, Bader analysis algorithm without lattice bias, J. Phys.: Condens. Matter 21 (2009), 084204.

[53] M. Yu, D.R. Trinkle, Accurate and efficient algorithm for Bader charge integration, J. Chem. Phys. 134 (2011), 064111.

[54] S. Yol Jeong, et al., Enhanced response and sensitivity of self-corrugated graphene sensors with anisotropic charge distribution, Sci. Rep. 5 (2015) 11216.

[55] S.-Y. Cho, H.-J. Koh, H.-W. Yoo, H.-T. Jung, Tunable chemical sensing performance of black phosphorus by controlled functionalization with noble metals, Chem. Mater. 29 (2017) 7197–7205.

[56] S.-Y. Cho, H.-J. Koh, H.-W. Yoo, J.-S. Kim, H.-T. Jung, Tunable volatile-organic-compound sensor by using Au nanoparticle incorporation on MoS$_2$, ACS Sens. 2 (2017) 183–189.

[57] S.-Y. Cho, S.J. Kim, Y. Lee, J.-S. Kim, W.-B. Jung, H.-W. Yoo, J. Kim, H.-T. Jung, Highly enhanced gas adsorption properties in vertically aligned MoS$_2$ layers, ACS Nano 9 (2015) 9314–9321.

[58] M. Yoosefian, N. Etminan, Leucine/Pd-Loaded (5,5) single-walled carbon nanotube matrix as a novel nanobiosensors for in silico detection of protein, Amino Acids 50 (2018) 653–661.

[59] J.-S. Kim, H.-W. Yoo, H.O. Choi, H.-T. Jung, Tunable volatile organic compounds sensor by using thiolated ligand conjugation on MoS$_2$, Nano Lett. 14 (2014) 5941–5947.

[60] D.M. Sim, M. Kim, S. Yim, M.-J. Choi, J. Choi, S. Yoo, Y.S. Jung, Controlled doping of vacancy-containing few-layer MoS$_2$ via highly stable thiol-based molecular chemisorption, ACS Nano 9 (2015) 12115–12123.

[61] M.R. Mananghaya, G.N. Santos, D. Yu, Solubility of aminotriethylene glycol functionalized single wall carbon nanotubes: a density functional based tight binding molecular dynamics study, J. Comput. Chem. 40 (2019) 952–958.